Journal of Colloid and Interface Science 576 (2020) 412–425

Contents lists available at ScienceDirect

Journal of Colloid and Interface Science

journal homepage: www.elsevier.com/locate/jcis

Direct conjugation of distinct carbon dots as Lego-like building blocks for the assembly of versatile drug nanocarriers

Yiqun Zhou [a], Keenan J. Mintz [a], Ling Cheng [a], Jiuyan Chen [a], Braulio C.L.B. Ferreira [a], Sajini D. Hettiarachchi [a], Piumi Y. Liyanage [a], Elif S. Seven [a], Nikolay Miloserdov [a], Raja R. Pandey [b], Bruno Quiroga [a], Patricia L. Blackwelder [a,c], Charles C. Chusuei [b], Shanghao Li [d], Zhili Peng [e,*], Roger M. Leblanc [a,*]

[a] Department of Chemistry, University of Miami, Coral Gables, FL 33146, USA
[b] Department of Chemistry, Middle Tennessee State University, Murfreesboro, TN 37132, USA
[c] GS/RSMAS, University of Miami, Key Biscayne, FL 33149, USA
[d] MP Biomedicals LLC, 3 Hutton Center, Santa Ana, CA 92707, USA
[e] School of Materials Science and Engineering, Yunnan Key Laboratory for Micro/Nano Materials & Technology, Yunnan University, Kunming, Yunnan 650091, China

GRAPHICAL ABSTRACT

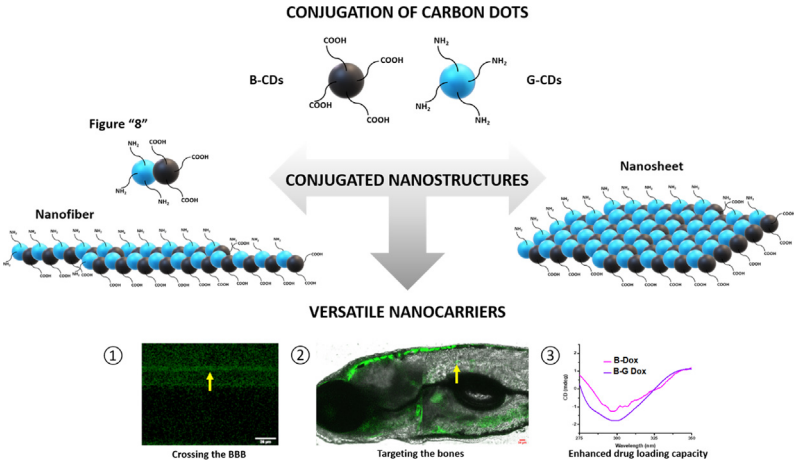

ARTICLE INFO

Article history:
Received 12 April 2020
Revised 27 April 2020
Accepted 2 May 2020
Available online 05 May 2020

Keywords:
Carbon dots
Conjugation
Nanocarrier
Bone targeting
Blood-brain barrier penetration
Drug loading

ABSTRACT

As a promising drug nanocarrier, carbon dots (CDs) have exhibited many excellent properties. However, some properties such as bone targeting and crossing the blood–brain barrier (BBB) only apply to a certain CD preparation with limited drug loading capacity. Therefore, it is significant to conjugate distinct CDs to centralize many unique properties on the novel drug nanocarrier. Considering that CDs have abundant and tunable surface functionalities, in this study, a direct conjugation was initiated between two distinct CD models, black CDs (B-CDs) and gel-like CDs (G-CDs) via an amidation reaction. As a result of conjugation at a mass ratio of 5:3 (B-CDs to G-CDs) and a two-step purification process, the conjugate, black-gel CDs (B-G CDs) (5:3) inherited functionalities from both CDs and obtained an enhanced thermostability, aqueous stability, red-shifted photoluminescence (PL) emission, and a figure-eight shape with a width and length of 3 and 6 nm, respectively. In addition, the necessity of high surface primary amine (—NH_2) content in the CD conjugation was highlighted by replacing G-CDs with other CDs with lower surface —NH_2 content. Meanwhile, the carboxyl groups (—COOH) on G-CDs were not enough to trigger

* Corresponding authors.
E-mail addresses: zhilip@ynu.edu.cn (Z. Peng), rml@miami.edu (R.M. Leblanc).

https://doi.org/10.1016/j.jcis.2020.05.005
0021-9797/© 2020 Elsevier Inc. All rights reserved.

self-conjugation between G-CDs. Moreover, the drug loading capacity was enhanced by 54.5% from B-CDs to B-G CDs (5:3). Furthermore, when the mass ratio of B-CDs to G-CDs was decreased from 5:30, 5:100 to 5:300, the obtained nanostructures revealed a great potential of CDs as Lego-like building blocks. Also, bioimaging of zebrafish demonstrated that various B-G CDs exhibited properties of both bone targeting and crossing the BBB, which are specific properties of B-CDs and G-CDs, respectively.

© 2020 Elsevier Inc. All rights reserved.

1. Introduction

Carbon dots (CDs) are a group of relatively new carbon-based spherical nanoparticles (NPs) with diameters less than 10 nm [1]. They are widely present in the nature [2] and can be also synthesized using various carbon-based substances as precursors by either top-down or bottom-up approaches [3–5]. They are well characterized for tunable surface functionality, excellent photoluminescence (PL), high photostability and water dispersity, good biocompatibility, and nontoxicity [6,7]. Also, they come in different sizes and surface chemistry depending on preparation methods and precursors applied [8,9]. Applications of CDs in drug delivery [10], bioimaging [11], sensing [5,12,13], optics [14], and other nanotechnology fields [15,16] are rapidly rising due to their aforementioned unique properties. However, the studies on CD surface chemistry properties are far from complete [17]. In fact, its tunable surface functionality also provides an opportunity to directly conjugate distinct CDs without extraneous polymer linkers [18].

It is of great significance to explore the properties of CD conjugates since particular properties only result from specific CD preparations [19,20]. Each CD preparation method has its own limitations. The strategy of binding distinct CDs is aimed at assembling novel versatile drug nanocarriers while passing on individual CD's merits within the nanostructures to compensate for deficiencies of each CD. For example, black CDs (B-CDs) and gel-like CDs (G-CDs) were both prepared in our lab from carbon nanopowder and citric acid, respectively [21,22]. B-CDs exhibited a unique bone targeting effect, but does not cross the blood–brain barrier (BBB), important for drug delivery to the central nervous system (CNS) [23,24]. In addition, carboxyl group (—COOH) (5.80×10^{-3} mmol/mg) is the only applicable functionality on the surface [22], which also limits the applications of B-CDs in drug delivery toward bones. In contrast, even though G-CDs didn't show any bone targeting effect [19], they can cross the BBB via passive diffusion. Moreover, they have plenty of primary amine groups (—NH_2) (8.47×10^{-2} mmol/mg) and other surface functionalities, such as hydroxyl (—OH) and carbonyl (C═O) groups [25], which are lacking for B-CDs but are advantageous for drug delivery. However, considering the low zeta potential (−13 mV) and self-aggregation revealed by atomic force (AFM) and transmission electron (TEM) microscopies [21], G-CDs don't have a high aqueous stability. Therefore, conjugating B-CDs and G-CDs gains the diversity of surface functionalities and aqueous stability needed to achieve both bone targeting effects, and the capability to cross the BBB. Generally speaking, we admit that there has been much work conducted in the assembly of nanostructures. For instance, Santos et al. utilized multivalent interactions to control supramolecular assembly of coated gold NPs (AuNPs) [26]. Markus Niederberger showed that ordered and disordered assembly of many inorganic NPs such as Fe_2O_3, CdTe, and AuNPs can occur through aggregation or electrostatic forces [27]. Cao and coworkers reviewed theoretical approaches for growing larger structures from NPs [28]. Additionally, some work incorporated CDs into a cross-linked network [29]. In contrast to the formation of CDs via covalent bonds, the stability of the CD conjugates and black-gel CDs (B-G CDs) reported in this work has enhanced properties over traditional NP assemblies which utilize electrostatic attraction or hydrogen bonding.

In this study, B-CDs and G-CDs were utilized as two distinct CD models. The presence of —COOH and —NH_2 on B-CDs and G-CDs, respectively, provided an easy access to their covalent conjugation. The conjugation of B-CDs and G-CDs was investigated by simple morphological studies combining AFM and TEM measurements. The surface functional groups of their conjugate, B-G CDs were studied with Fourier-transform infrared (FTIR) and X-ray photoelectron spectroscopies (XPS). Specifically, the —NH_2 group was quantified via a fluorescamine assay, which was again used to confirm whether the conjugation was successful while revealing possibilities to conjugate B-G CDs with —COOH containing drugs for future drug delivery. The optical properties of B-G CDs were studied with UV/vis absorption and fluorescence emission spectroscopies. The thermostability and aqueous stability of B-G CDs were analyzed with thermogravimetric analysis (TGA) and zeta potential measurements, respectively. Subsequently, the drug loading capacity of B-G CDs was evaluated in comparison to B-CDs and G-CDs with the help of circular dichroism spectroscopy. Doxorubicin (Dox) was selected as a drug model due to its chirality and significance in the treatment of tumors [30].

In addition, to investigate the factors affecting successful conjugation (such as the density of surface —NH_2 groups) and explore the universality of CDs as building blocks, G-CDs were replaced with yellow CDs (Y-CDs) (having a markedly lower surface —NH_2 density) to examine conjugation effects with B-CDs. Also, the possibility of self-conjugation between G-CDs was investigated via the same N-(3-dimethylaminopropyl)-N′-ethylcarbodiimide hydrochloride/*N*-hydroxysuccinimide (EDC/NHS) coupling, and a series of subsequent spectroscopic and microscopic characterizations. Furthermore, in order to confirm the availability of CDs as building blocks for novel nanostructures, we conducted a parallel experiment by decreasing the mass ratio of B-CDs and G-CDs from 5:3, 5:30, 5:100 to 5:300 to achieve novel nanostructures, which were also examined by a series of spectroscopic and microscopic characterizations to study the optical properties and morphologies of the new B-G CDs. Moreover, various B-G CDs were independently injected into the yolk sac and heart of zebrafish to study whether they obtained both capabilities of bone targeting and crossing the BBB from B-CDs and G-CDs, respectively, through their conjugation. This research is creative and original because it proposes the unprecedented idea that CDs could be directly conjugated to each other in a way similar to organic molecules. Among various NPs, the development of biocompatible carbon-based nanomaterials is a popular trend considering their nontoxic nature and excellent properties that meet the demand of various applications. CDs obtained from distinct preparations may serve as customizable Lego-like building blocks. The assembled nanostructures adopt properties from its different precursors, enabling the CD conjugate to become a versatile drug nanocarrier, and potentially expanding its for diverse future applications.

2. Experimental

2.1. Materials

To synthesize and purify B-CDs, carbon nanopowder (<100 nm) was purchased from Sigma-Aldrich (St. Louis, MO, USA). Sulfuric acid (98%) and nitric acid (68–70%) of ACS grade were bought from ARISTAR (distributed by VWR, Radnor, PA, USA). Sodium hydroxide (NaOH) and chloroform of ACS grade were provided by MP biomedicals (Irvine, CA, USA). Dialysis bag with molecular weight cut-off (MWCO) of 3500 Da was acquired from Thermo Scientific (Rockford, IL, USA). To prepare and purify G-CDs, citric acid (99.5–100%) and acetone (99.9%) were bought from VWR (West Chester, PA, USA), and 1,2-ethylenediamine (EDA) (≥99.0%) was purchased from MP Biomedicals (Irvine, CA, USA). Compressed argon gas with ultra-high purity was ordered from Airgas (Miami, FL, USA). For the synthesis and purification of Y-CDs, citric acid (99.5–100%) and 1,2-phenylenediamine (OPD) flakes (99.5%) were obtained from VWR (West Chester, PA, USA) and Sigma-Aldrich (St. Louis, MO, USA), respectively. Sephacryl S-300 was bought from GE Healthcare (Uppsala, Sweden) as the matrix for *SEC*. In addition, EDC (≥99.0%), NHS (97.0%) and fluorescamine (98%) were purchased from Sigma-Aldrich (St. Louis, MO, USA). Quinine hemisulfate monohydrate (99%) was obtained from Alfa Aesar (Heysham, England). Dox (>95%) was bought as doxorubicin hydrochloride from (Tokyo, Japan). The deionized (DI) water used was purified using a Modulab 2020 water purification system acquired from Continental Water System Corporation (San Antonio, TX, USA). It had a pH of 6.62 ± 0.30, surface tension of 72.6 $mN{\cdot}m^{-1,}$ and a resistivity of 18 MΩ·cm at 25.0 ± 0.5 °C. All the chemicals were used as received.

2.2. Syntheses of various carbon dots

B-CDs, G-CDs and Y-CDs were synthesized as described in our previous work [20–22]. To be specific, the synthesis of B-CDs was initiated with 9 mL sulfuric acid and 3 mL nitric acid added to 250 mg carbon nanopowder in a round-bottom flask. The mixture was heated with vigorous stirring and refluxing to 110 °C for 15 h in a sand bath. After cooling down to room temperature, oversaturated NaOH aqueous solution was added to neutralize the acidic solution in an ice bath. With the addition of oversaturated NaOH, salts such as Na_2SO_4 and $NaNO_3$ immediately formed as precipitates. Then the mixture was filtered three times to remove unreacted carbon nanopowder, formed salts and yield a dark-brown aqueous solution. The aqueous solution was transferred to a beaker and concentrated by reducing the volume to about 25 mL using a hotplate with the temperature controlled at 75–85 °C. Subsequently, the aqueous solution was cooled down in an ice bath to remove again the salt crystals and obtain the dark brown supernatant solution, which was followed by the addition of 15 mL chloroform to extract organic impurities three times. The aqueous phase was decanted and centrifuged at 3000 rpm for 30 min to remove any precipitates before it was transferred to a dialysis bag (MWCO: 3500 Da), and dialyzed against 4 L of DI water for 5 days. The DI water was replaced every 4–10 h. Finally, the aqueous solution kept in the dialysis bag was concentrated using a rotary evaporator to yield 27.4 mg B-CDs as a black powder.

In the beginning of G-CD production, argon gas was applied for 5 min to remove O_2 from the solvothermal synthesis system. Then, 5 mL EDA was transferred into a 50-mL round-bottomed flask, which was heated with vigorous stirring and refluxed in an oil bath on a hotplate. When the temperature reached 160 °C, 1 g of citric acid was added into the boiling EDA. With vigorous stirring and refluxing, the reaction proceeded for 50 min to allow for citric acid to completely react with EDA. Argon gas was used throughout the entire reaction to prevent EDA from being oxidized. After the system was cooled down to room temperature, G-CDs were present at the bottom of the flask. Meanwhile, the supernatant unreacted EDA was extracted with 10 mL acetone three times and discarded. Subsequently, the G-CDs (0.8 g) were dispersed in water (1 mL), and processed by vacuum evaporation at a relatively constant temperature, between 70 to 80 °C. Then G-CDs would form under these conditions.

The synthesis of Y-CDs utilized 0.02 g citric acid and 0.28 g OPD as the carbon source and *N*-dopant, respectively. Initially, they were dissolved and mixed in a 20 mL test tube that contained 10 mL DI H_2O. In an ultrasonication bath, the mixture was sonicated at a frequency of 42 kHz for 1 h under an argon gas blanket. An orange solution was then obtained showing yellow emission under a UV lamp (365 nm). After filtration of unreacted OPD three times in an ice bath and removal of small fluorophores by *SEC*, Y-CDs remained in aqueous solution. After lyophilization, Y-CDs were obtained as a brown powder.

2.3. Preparation of carbon dot conjugates

The conjugation of B-CDs and G-CDs was initialized by adding 5 mg of B-CDs into a 100 mL round-bottom flask and then dissolved in 2 mL of phosphate-buffered saline solution (PBS) (pH 7.4). Sonication was performed to ensure that B-CDs were well dispersed. Then, approximately 11.1 mg of EDC was dissolved in 1 mL of PBS, and added to the flask. The solution was then stirred constantly for 30 min using a small stirring rod. Later, about 6.67 mg of NHS was dissolved in 1 mL of PBS and added to the flask. The solution was stirred for another 30 min. In the end, 3, 30, 100 or 300 mg of G-CDs was dissolved in 1 mL of PBS and added to the solution containing (B-CDs, EDC and NHS) which was then stirred overnight. The conjugation of B-CDs and Y-CDs was similar to the conjugation of B-CDs and G-CDs. In detail, 1 mg of B-CDs and 2.22 mg of EDC were dispersed or dissolved in 2 mL of PBS and stirred for 30 mins. Then, 1.34 mg of NHS was dissolved in 2 mL of PBS, added to the solution and stirred for another 30 min. In the end, 50 mg of Y-CDs was dispersed in PBS, added to the solution containing B-CDs, EDC and NHS, and stirred overnight.

2.4. Microscopy

The morphology of CDs conjugates was characterized by a combination of AFM and TEM measurements. AFM measurements were performed using an Agilent 5420 atomic force microscope. Prior to AFM imaging, one drop of a conjugated CD aqueous dispersion (0.1 mg/mL) was dropped onto a clean silica mica slide, which was followed by screening with tapping mode AFM. TEM images were obtained from a JEOL 1400× TEM with a drop of conjugated CD aqueous dispersions (0.1 mg/mL) placed on each carbon-coated 200 mesh copper grid and air dried. For scanning electron microscopy (SEM) preparation, the conjugated CDs in a solid state were placed on aluminum stubs covered with a carbon adhesive tab. Samples were then viewed in a Philips XL-30 field emission SEM, and images were digitally collected. Confocal microscopy was performed using a Leica SP5 confocal microscope with objective magnifications of 25× and 70× for the bone targeting experiment, and 90× to examine CDs crossing the BBB.

2.5. Spectroscopy

A Cary 100 UV/vis spectrophotometer was applied to record UV/vis absorption spectra of CDs conjugates in a 1 × 1 cm quartz cuvettes. A Fluorolog (Horiba Jobin Yvon) spectrometer and a Varian Cary Eclipse spectrometer were used to obtain fluorescence

emission spectra and fluorescence quantum yield (QY) of CDs conjugates with a 1 × 1 cm quartz cuvette, and a slit width of 5 nm for both excitation and emission. FTIR spectral data were acquired from a Perkin-Elmer Frontier FTIR spectrometer equipped with attenuated total reflectance accessories using air as background. XPS was performed using a Perkin-Elmer PHI 560 system with a double-pass cylindrical mirror analyzer operated using a Mg Kα anode with a hυ = 1253.6 eV photon energy operated at 250 W and 13 kV. B-G CD samples were mounted as a powder onto a custom-built sample holder and inserted into the XPS system via turbopumped antechamber. The observed C 1s core level at 284.9 eV emanating from the C=C alkenyl B-G CD as previously measured in our laboratory [17,25,31,32] was used as a binding energy (BE) reference. Core level intensities of the O 1 and C 1s orbitals were normalized using their known atomic sensitivity factors [33]. XPS peaks were curvefitted using 70%-to-30% Gaussian-Lorentzian lineshapes with Shirley background subtractions [34]. BE peak envelopes were deconvoluted using CasaXPS ver. 2.2.107 (Devonshire, UK) software. Zeta potentials were measured by Malvern Zetasizer Nano equipment, and all samples were measured in aqueous dispersion at room temperature. The TGA was conducted using a Netzsch TG 209 F3 Tarsus thermo-microbalance while heating under a flow of air gas from 30 to 1000 °C at a rate of 10 K/min. Circular dichroism spectroscopy was performed with the use of a JASCO J-810 spectropolarimeter and a quartz cuvette with the pathlength of 1 mm.

3. Results and discussion

3.1. Preparation of black-gel carbon dots

Although both B-CDs and G-CDs have abundant —COOH and —NH_2 groups on their respective surfaces, the formation of peptide bonds through —COOH and —NH_2 is challenging and usually hinges on heating or incorporation of enzymes. In this study, similar to the process of drug loading on B-CDs, the conjugation of B-CD and G-CDs utilized a classic EDC/NHS coupling reaction. The abundant —COOH on the surface of B-CDs provides advantageous conditions for initializing the conjugation. With the addition of EDC, it reacted with the equivalent amount of —COOH groups to form an unstable o-acylisourea intermediate, which was easily displaced by an equivalent amount of NHS to form a much more stable ester-intermediate. However, the most favorable condition of EDC crosslinking is acidic. Therefore, when the CDs conjugation was performed in PBS, the amount of EDC and NHS was increased by 1.5–2 fold to compensate for the reduced efficiency and yield more intermediates with B-CDs as the limiting reagent. In the end, when a higher quantity of G-CDs was added into the mixture, the intermediates were displaced by rich surface —NH_2 groups of G-CDs. The final products, B-G CDs, were obtained via a S_N2 nucleophilic substitution reaction. A schematic representation of the conjugation process of B-CDs and G-CDs is illustrated in Scheme 1.

3.2. Purification of carbon dot conjugates

In order to completely purify the B-G CDs, a two-step purification process was applied. First, the obtained mixture was dialyzed against DI water for 3 days with a dialysis bag (MWCO = 3500 Da) to remove excess G-CDs considering their low molecular weight (319 g/mol) [21]. In the second step, any unreacted B-CDs were separated from the B-G CDs by size-exclusion chromatography (*SEC*) using a GE Healthcare Sephacryl S-300 (Uppsala, Sweden) and DI water as the stationary and mobile phases, respectively. In contrast, separation of the mixture was also performed by electrophoresis and thin-layer chromatography (TLC) based on differences in surface charge and polarity, respectively. However, electrophoresis and TLC techniques were not successful in separating B-CDs and B-G CDs (Fig. S1). Based on the separation principle of *SEC*, the B-G CD was the first colorless eluent due to an increased particle size whereas B-CDs dispersion was collected as the second brown eluate. For higher separation efficiency, each eluate was collected with several test tubes and the sample in each test tube was analyzed by both UV/vis absorption and fluorescence emission spectroscopies to confirm the separation of B-CDs and B-G CDs. After careful identification and collection of the B-G CDs, mass spectrometry was performed on the conjugate using both electrospray ionization (ESI) and matrix-assisted laser desorption/ionization-time of flight (MALDI-TOF) techniques. In the ESI mass spectrum (Fig. S2a), the highest peak is at 337 g/mol. In comparison to the highest peak in the mass spectrometry of G-CDs (319 g/mol), the addition of 18 g/mol could be assigned to the ionized fragment of the peptide bond formed during the conjugation of B-CDs and G-CDs, which is confirmed by the addition of 17 g/mol by comparing the MALDI-TOF mass spectra of B-G CDs (Fig. S2b) and B-CDs [35]. To purify the B-Y CDs, after stirring overnight, the aqueous dispersion was put in dialysis bag against DI water (MWCO: 3500 Da) for 3 days. The resulting orange fluorescent eluate was collected after running the colloidal suspension through a *SEC* column. The collected solution was finally processed by lyophilization to obtain the solid product.

3.3. Characterization of black-gel carbon dots

After lyophilization, pure B-G CDs were prepared as an aqueous dispersion at a predetermined concentration for optical property studies (UV/vis, fluorescence, FTIR) and XPS measurements. The UV/vis absorption spectrum (Fig. S3a) exhibits two shoulder peaks at 228 and 275 nm that are similar to those UV/vis spectra of B-CDs

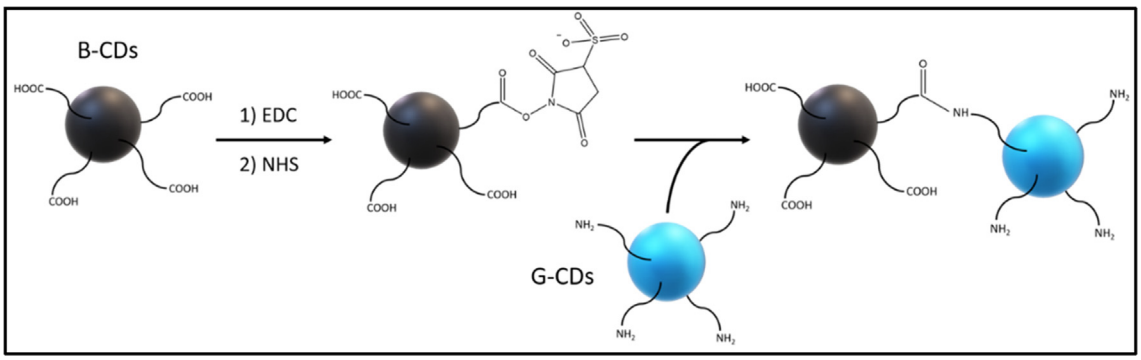

Scheme 1. The conjugation of B-CDs and G-CDs via an EDC/NHS mediated amidation reaction.

alone and the mixture of B-CDs and G-CDs (Fig. S3b), which are assigned to C=C π-π* and C=O n-π* transitions, respectively [22]. The fluorescence emission spectrum (Fig. 1a) shows the maximum excitation and emission wavelengths of B-G CDs at 325 and 504 nm, respectively. Meanwhile, the emission wavelengths achieved upon the excitation of the maximum excitation

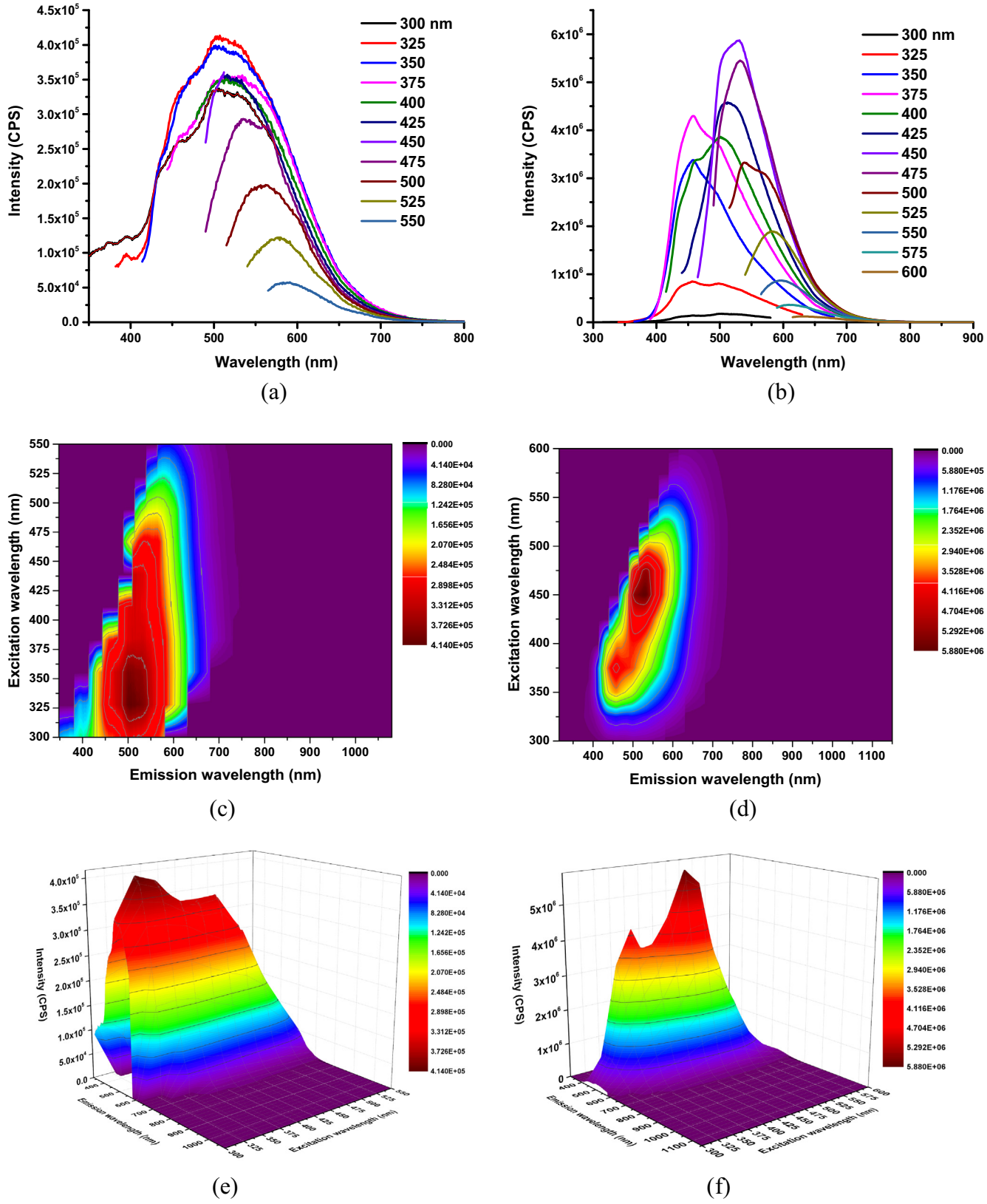

Fig. 1. Fluorescence emission spectrum of B-G CDs aqueous dispersion (0.1 mg/mL) (a), and the aqueous dispersion mixture of B-CDs (0.25 mg/mL) and G-CDs (0.15 mg/mL) (b). 2D (c) and 3D (e) plots of the excitation emission spectrum of B-G CDs aqueous dispersion. 2D (d) and 3D (f) plots of the excitation emission spectrum of mixed aqueous dispersion of B-CDs and G-CDs.

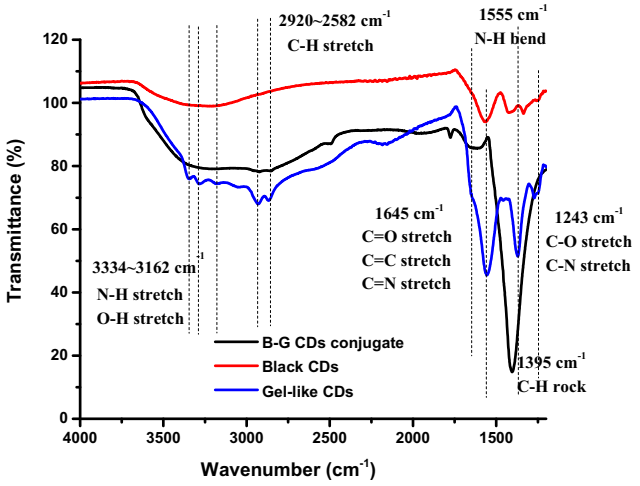

Fig. 2. The comparison of FTIR spectra of B-CDs, G-CDs and B-G CDs with air as background.

wavelengths of B-CDs (450 nm) and G-CDs (350 nm) are 520 and 450 nm, respectively. In comparison, the maximum excitation wavelength of B-G CDs is shortened but the corresponding emission falls in between that of B-CDs and G-CDs alone and tends to have long wavelength. Additionally, the 2D (Fig. 1c) and 3D (Fig. 1e) plots of the excitation emission spectrum of B-G CDs indicate a single emitter. In contrast, the fluorescence emission spectrum (Fig. 1b), 2D (Fig. 1d) and 3D (Fig. 1f) plots of the excitation emission spectrum of B-CDs and G-CDs mixture shows two emission regions that correspond to the separate emission spectrum of B-CDs and G-CDs alone. Therefore, the conjugation between B-CDs and G-CDs was further confirmed by the fluorescence spectroscopy. In addition, the fluorescence QY of B-G CDs was measured with quinine sulfate dissolved in 0.1 M H_2SO_4 solution as the standard and substantially decreased by 98% in comparison to that of G-CDs alone (40%). It was reported by Madani et al. that direct coupling results in the fluorescence quenching which can be affected by the CD size, concentration, and the distance between distinct CDs [36]. Specifically, when two CDs get closer, their sizes decrease so that their surface area to volume ratio will be increased, or their concentrations increase, the fluorescence quenching becomes more prominent. Furthermore, when two CDs are connected, Förster resonance energy transfer (FRET) may occur, which means one CD in its excited state will transfer energy to the other CD through nonradiative dipole-dipole coupling [37]. And the FRET efficiency will be enhanced by shortening the distance of two CDs [38] and the role (donor or acceptor) each CD plays will be determined by the overlap of their UV/vis absorption and fluorescence emission spectra. Fig. S4 shows that the absorption peak of B-CDs overlaps with the emission peak of G-CDs excited at 350 nm, but the absorption peak of G-CDs doesn't overlap with the emission peak of B-CDs excited at 350 nm. This effect demonstrates that when FRET occurs, G-CDs are donors while B-CDs serve as acceptors, which also explained the low fluorescence QY of the B-G CDs.

From the FTIR spectrum (Fig. 2), we observe a broad —OH peak for B-CDs between 3334 and 3162 cm^{-1} while G-CDs have sharp —NH_2 peaks in the same region [22]. In addition, due to the presence of EDA fragment on the surface of G-CDs, there exist peaks at 2920–2582 and 1555 cm^{-1} that correspond to the C—H stretch and N—H bend of EDA, respectively [21]. In contrast, after conjugation, B-G CDs show peaks corresponding to the —OH stretch, C—H stretch and N—H bend from EDA, which confirms the successful conjugation of B-CDs and G-CDs on a structural basis and reveals that B-G CD obtained versatile surface functionalities through conjugation. Furthermore, the abundance of hydrophilic functionalities on the surface endows the B-G CDs with excellent hydrophilicity compared to their predecessors.

Fig. 3 shows XPS core levels for the C 1s, N 1s and O 1s orbitals of the B-G CDs. Atom % mole fractions of C and O were 70.5 and 29.5%, respectively. It should be noted that extended scans were required to achieve sufficient signal/noise (S/N) of the N 1s signal for its detection and analysis (measured atom % N < 0.01%). Considering the wide and low resolution (and accompanying linewidth broadening) of the weak N 1 peak (full width at half maximum (fwhm) = 3.0 eV), we assign the BE peak center at 398.4 eV to —NH_2 [25,39]. The high C 1s BE at 289.3 eV is comparable with carboxylate groups (—COO-) as previously observed [40]. BEs denoting the conjugate sp^2 structure and —COO— (with fwhm in parentheses) are at 284.9 (2.4) and 289.3 (3.3) eV, respectively. Based on integrated C 1s peak areas, the C=C to —COO— ratio on the B-G CD surface is 3.4:1. It should be noted that given the relatively large fwhm at 289.3 eV, there are likely unresolved oxidation states present. The O 1s core levels for this sample show BE peak centers (with fwhm in parentheses) at 531.3 (2.4) and 532.7 (2.5) eV, consistent with C=O [41] and an O-containing polymeric structure [42], respectively. The relative C=O to polymeric O ratio, based on relative integrated peak areas of the O 1s orbital, is 1:4.5.

In addition, the content of —NH_2 on the surface of B-G CDs is calculated based on an fluorescamine assay with G-CDs as the reference (Fig. S5a). Since a linear relationship has been observed between the concentration of —NH_2 groups and fluorescence intensity using EDA as a standard [25], the surface —NH_2 content of B-G CDs was calculated to be 1.68 × 10^{-2} mmol/mg which is ~20% of that of G-CDs. Considering the presence of B-CD fragment, a titration against NaOH aqueous solution was carried out for the quantification of —COOH groups present on the as prepared B-G CDs. Initially, an aqueous dispersion of 1 mg/mL B-G CDs was prepared in DI water. However, upon addition of the visual indicator, phenolphthalein, the solution instantly turned pink (Fig. S5b),

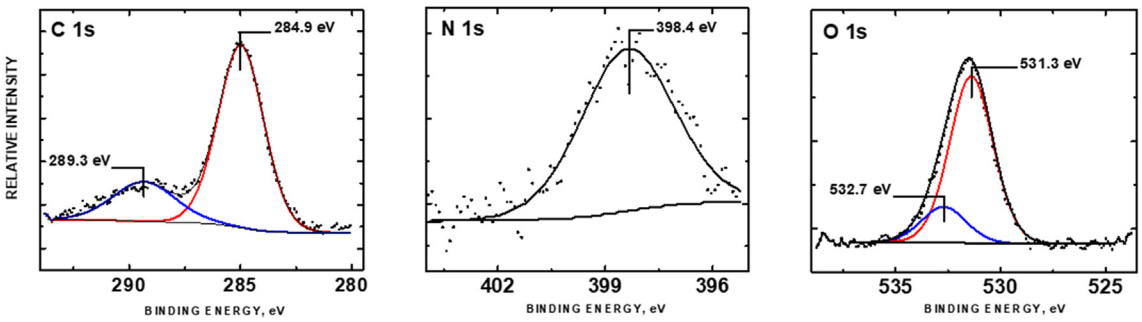

Fig. 3. XPS core levels of C 1s, N 1s and O 1s orbitals of the B-G CDs.

indicating that the B-G CD aqueous dispersion is basic. Thus, the acid-base titration reveals that the surface of B-G CD is dominated by —NH_2 groups, and the quantification of —COOH with lower surface content can't be achieved with classical methodologies.

Prior to AFM and TEM, ultrasonication usually was needed to avoid self-aggregation of CDs. However, when B-G CDs were characterized by AFM and TEM, ultrasonication seemed unnecessary since the same AFM or TEM images before (Fig. S6) and after ultrasonication were obtained, revealing the stability of B-G CDs in water. In Fig. 4a, the figure-eight shape of the conjugate can be clearly seen by AFM. The height of these particles (2–3 nm) correlates with the height range of the B-CDs and G-CDs alone in the z-axis [21,22]. In Fig. 4b, the TEM image shows the same shape observed in the AFM image (inset), with some variety, which confirm conjugation in comparison to the spherically shaped B-CDs and G-CDs alone (Fig. S7). Some of the particles appear to have a bent shape, which indicates three CDs conjugated together. Many particles exhibit a round shape, which may be due to either: (1) a vertical orientation of the conjugated particles which do not show the same figure-eight shape as expected, or (2) that there still exist many single CDs. The size distribution of 3.8 ± 0.8 nm correlates with size distributions of the conjugated CDs with a slight

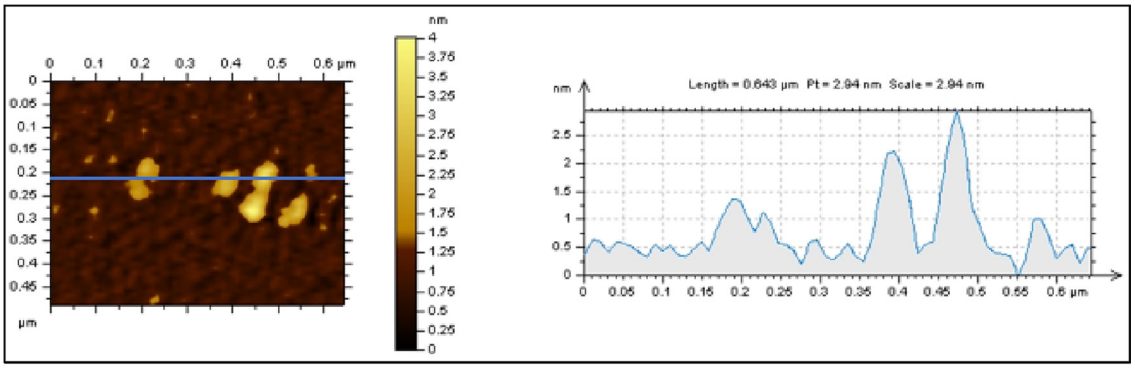

(a)

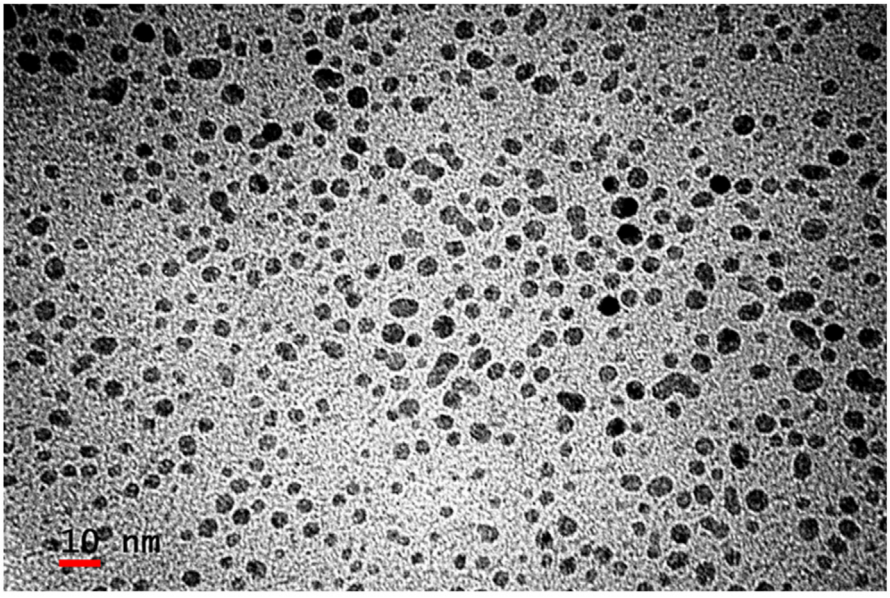

(b)

Fig. 4. (a) AFM and (b) TEM images of B-G CDs (0.1 mg/ml) with 2-min ultrasonication treatment. Scale bar in the TEM image represents 10 nm. Histogram of particle size distribution measuring the shortest diameter of particles.

size increase and the deformation might result from the rearrangement of surface functionalities during the conjugation process.

TGA was performed on B-CDs, G-CDs, and their conjugate to compare their thermal stabilities. The TGA spectrum of B-CDs in Fig. S8a shows four decomposition stages. Initially, the weight loss of B-CDs was 18% at 200 °C due to the evaporation of water molecules adsorbed by B-CDs [43,44]. As the temperature was increased from 200 to 440 °C, the weight loss was 22%, which might be caused by the decomposition of organic functional groups especially oxygen-containing groups on the surface of B-CDs and release of water and CO_2 [45,46]. When B-CDs were heated from 440 to 634 °C, there was barely any mass loss. In comparison, carbon nanopowders, the precursor of B-CDs, were largely decomposed in this temperature range due to their amorphous structure. Nevertheless, between 634 and 900 °C, there was a large mass loss of 27% for B-CDs, most likely due to the combustion of the graphite crystalline core of B-CDs and release of pyrogas [44,47]. The high residue mass at 26% may indicate the presence of some hard-combustible residues. In comparison, the TGA measurement of G-CDs in Fig. S8b indicates four decomposition stages. For better identification of each decomposition stage, TGA was also performed on the precursors of G-CDs, namely citric acid and EDA. The first stage (30–116 °C) is characterized by a mass loss of 15%, which is related to the desorption of water and remaining EDA molecules on the surface of G-CDs considering the boiling point (116 °C) of EDA [45]. The second stage (116–200 °C) closely follows the first stage and is accompanied by a significant mass loss of 41%, which might be due to the evaporation of water adsorbed by G-CDs and partial decomposition of the external surface of G-CDs [43,44,48]. The third stage (200–470 °C) does not result in a large mass loss, which is only 20% potentially due to the loss of capping molecules such as citric acid regarding the boiling point (310 °C) of citric acid or smaller G-CDs [48]. The last stage (470–573 °C) again results in a significant mass loss of 23% without any residue left, which indicates the complete decomposition of G-CDs and amorphous carbon core [49]. The TGA spectrum of B-G CDs, even though has many indefinite stages at 30–200, 200–500, 500–700, and 700–900 °C accompanied by a total mass loss of 81% (Fig. S8c), shows the highest decomposition peak at 703 °C which is clearly higher than that of both B-CDs (634 °C) and G-CDs (470 °C), which we attribute to enhanced thermostability caused by a strengthened structure through conjugation.

Zeta potential is an important indicator of the surface electrical properties of CDs through investigations of the charge on the surface of CDs as well as their aqueous stability. Based on our previous measurements, both B-CDs and G-CDs have shown negative surface charges with mean zeta potential values of −38.0 and −13.0 mV, respectively. This finding suggests that B-CDs are considerably more stable than G-CDs in water. However, after conjugation, the improved aqueous stability of B-G CDs was observed by previous AFM and TEM measurements, which was also confirmed by the increasing mean zeta potential value (-31.6 mV) of B-G CDs. Also, the proximity of zeta potentials of B-CDs and B-G CDs further explains the difficulty faced in separation using electrophoresis. In contrast, a mixed solution containing 5 mg B-CDs and 3 mg G-CDs in 5 mL water exhibits a mean zeta potential value of −43.1 mV, providing further support for successful conjugation.

3.4. The effect of primary amine and carboxyl surface functional groups on carbon dot conjugation

In order to investigate the effect of $—NH_2$ surface density on the CD conjugation, we replaced the G-CDs by another type of CDs, Y-CDs to explore the possible conjugation with B-CDs. Y-CDs were prepared via an ultrasonication-mediated bottom-up approach with citric acid and OPD as precursors [50]. The content of $—NH_2$ on the surface of Y-CDs is 3.75×10^{-2} mmol/mg [50], which is about 44% of the $—NH_2$ content on the surface of G-CDs [25]. Therefore, the efficiency of conjugating B-CDs with Y-CDs should be much less than that of the conjugation of B-CDs and G-CDs. This hypothesis has been confirmed by both UV/vis absorption, fluorescence emission spectra and the TEM image in Fig. S9. Both UV/vis absorption (Fig. S9a) and fluorescence emission (Fig. S9b) spectra of the B-Y CDs are similar to those of B-CDs while the TEM image (Fig. S9c) shows most of the NPs have a spherical shape in contrast to the figure-eight shape observed in the B-G CDs. Thus, while the conjugation of B-CDs and Y-CDs was most likely unsuccessful, it reveals that the $—NH_2$ surface density plays a vital role in the conjugation of two distinct CDs.

In addition, except for $—NH_2$, characterization of G-CDs in previous studies also revealed the presence of carboxylates so the EDC/NHS chemistry might trigger a self-conjugation of G-CDs. To investigate whether a G-CD can conjugate with another G-CD, the same conjugation procedure was followed except the addition of B-CDs. To purify the possible conjugate (G-G CDs), two different dialysis bags (MWCO: 100–500 and 3500 Da) were applied for a 3-day dialysis. After careful purification and lyophilization, trace amounts of possible G-G CDs was obtained following each purification step. However, UV/vis absorption, fluorescence emission and FTIR spectroscopic data (Figs. S10 and S11) confirmed that the possible G-G CDs share the same optical or structural properties as the G-CDs purified with dialysis in both MWCO but different from those of B-G CDs. In addition, AFM images in Fig. S10 showed that G-G CDs are generally spherical with a mean diameter of 2 nm, which is similar to that of G-CDs alone. Therefore, even though carboxylates were observed on the G-CDs, the amount of carboxylates might not be sufficient to trigger self-conjugation between G-CDs to form G-G CDs. So, in terms of conjugation sequence, B-CDs might conjugate with G-CDs alternately.

3.5. Drug loading capacity

CDs have been widely utilized as drug nanocarriers due to their excellent properties such as abundant surface functionalities and large surface area to volume ratio, which are significantly enhanced during the conjugation of B-CDs and G-CDs. Meanwhile, the drug loading capacity was evaluated by conjugating various nanocarriers (B-CDs, G-CDs and B-G CDs) with Dox and performing circular dichroism analysis on both bare nanocarriers and their conjugates to Dox.

After conjugation overnight via EDC/NHS mediated amidation reactions and purification through dialysis (conjugation and purification procedures are presented in the supporting information), all conjugates between Dox and various nanocarriers, namely B-CDs (B-Dox), G-CDs (G-Dox), and B-G CDs (B-G-Dox), were investigated by both fluorescence and FTIR spectroscopies (Fig. S12). Fluorescence spectroscopic data show that the fluorescence spectra of G-Dox (Fig. S12b) were composed of the fluorescence spectra of G-CDs [21] and Dox (Fig. S12a), independently, which suggests unsuccessful conjugation between G-CDs and Dox. The presence of Dox (positive charge) may be due to an electrostatic interaction with G-CDs (negative charge). The spectra of B-Dox (Fig. S12c) are similar to that of B-CDs [22]. Even though the peak of Dox at around 600 nm can be observed, the conjugation between B-CDs and Dox needs further confirmation. Compared to the spectra of G-Dox and B-Dox, the spectra of B-G-Dox (Fig. S12d) display two emission areas that correspond to B-G CDs and Dox, among which the emission of Dox appears predominant. In contrast to the fluorescence spectra of B-G CDs (Fig. 1a), a hypsochromic shift was observed in the B-G CDs emission area in the spectra of B-G-Dox (Fig. S12d) caused by the conjugation of B-G CDs and Dox. Therefore, B-G CDs were successfully conjugated to Dox. FTIR spectra

of Dox, G-CDs, G-Dox (Fig. S12e) and Dox, B-G CDs, and B-G-Dox (Fig. S12g), which confirm our previous statements. Moreover, the FTIR spectrum of B-Dox (Fig. S12f) present characteristic information from both Dox and B-CDs, which confirms conjugation between B-CDs and Dox.

When the drug (Dox) loading capacity was studied by performing circular dichroism analyses, it turned out that all bare nanocarriers showed no peaks (Fig. S13a), which demonstrated all nanocarriers to be achiral. Nonetheless, Dox has chiral centers which provided polarized light rotation and generated circular dichroism peaks at 300, 350 and 450 nm as shown in Fig. S13b. Thus, when Dox is loaded on any bare nanocarriers via covalent conjugation, circular dichroism signals should be detected on various CD-Dox conjugates. In addition, the peak intensity at 300 nm increases over the mass concentration of Dox in a linear relationship (R^2 = 0.94) (Fig. S13b), which lays the foundation for quantifying the amount of Dox loaded on various nanocarriers. Circular dichroism analyses of B-Dox, G-Dox and B-G-Dox (Fig. 5) depict that in comparison to that of B-Dox and B-G-Dox, the circular dichroism spectrum of G-Dox shows no signal, which again demonstrates that Dox was hardly loaded onto the G-CDs since covalent conjugation between G-CDs and Dox relies on the amidation reaction of —NH_2 and —COOH which is lacking in both G-CDs and Dox. The comparison between B-Dox and B-G-Dox shows that B-G-Dox has a higher peak intensity than B-Dox at 300 nm. With the molecular weights (B-G-Dox: 953.45 g/mol; B-Dox: 715.83 g/mol) obtained from mass spectrometry and actual mass concentrations (B-G-Dox: 0.165 mg/mL; B-Dox: 0.105 mg/mL) taken into consideration, the molar concentrations of B-Dox and B-G-Dox are close. It is noteworthy that even though their molar concentrations are similar in the same volume (2 mL), the peak intensity of B-G-Dox at 300 nm shows a 54.5% increase as compared to that of B-Dox, which suggests a significant 54.5% increase of drug (Dox) loading capacity achieved through the conjugation between B-CDs and G-CDs. This further supports the enhanced drug loading capacity via conjugation of B-CDs and G-CDs which was previously revealed by the predominant Dox emission in the fluorescence spectra of B-G-Dox (Fig. S12d) and might be ascribed to increased surface area to volume ratio, and strengthened electrostatic interaction or covalent conjugation due to the increased surface functionalization.

3.6. The availability test of carbon dots as building blocks for novel nanostructures

CDs are viable building blocks for novel nanostructures. Even though we showed that the conjugation between B-CDs and G-CDs to generate the figure-eight shaped B-G CDs, in order to further test the availability of these CDs as building blocks to assemble novel nanostructures, we varied the initial reaction mass ratio of B-CDs:G-CDs from 5:3 to 5:30. By increasing the amount of G-CDs, the new B-G CDs (5:30) exhibit similar properties to G-CDs. For instance, when the fluorescence emission spectroscopy was performed on the B-G CDs (5:30), the spectrum (Fig. S14b) recorded the maximum excitation to be 325 nm, which is the same as that for B-G CDs (5:3). However, the corresponding emission wavelength possesses a blue shift as compared to the previous conjugation. The emission peak at 432 nm is much closer to that of 450 nm obtained from G-CDs upon the excitation of 350 nm. In addition, the UV/vis absorption spectrum (Fig. S14a) of B-G CDs (5:30) shows a single peak at 265 nm that corresponds to the C=O n-π transition or C=C π-π* transition, which is different from B-CDs, G-CDs, and the B-G CD (5:3). In terms of morphology, the B-G CDs (5:30) were characterized by a combination of AFM and TEM. From the AFM image (Fig. 6a), the B-G CDs (5:30) appear as mostly irregularly shaped NPs, and the shapes achieved include figure-eight, bent and other irregular shapes due to the conjugation of more CDs. The height of these NPs ranges between 4 and 6 nm, which is double of that of B-G CDs (5:3) and suggests multiple conjugation. To confirm the AFM result, TEM was performed. We again observed in panel i of the TEM image (Fig. 6b) that the B-G CDs (5:30) were composed of many irregular-shaped NPs, including figure-eight shapes as observed in the B-G CDs (5:3). Panel ii of Fig. 6b illustrates the three most repetitive and distinguishable shapes found in TEM with schematic diagrams beside them to clarify the variety of nanostructures obtained from CD conjugation. In detail, the first figure shows a NP with a round shape but dark color, which might be due to a vertical orientation of figure-eight shaped conjugate. The second figure exhibits the conjugate with a figure-eight shape. The third figure shows a novel nanostructure formed by a multiple conjugation which is also the most common shape obtained in the conjugation of 5:30.

When the mass ratio of B-CDs: G-CDs continued to decrease from 5:30 to 5:100 and 5:300, the morphology of B-G CDs became more varied. The AFM image (Fig. 7a) shows many clusters formed by B-G CDs (5:100). The height dramatically increases up to about 25 nm which is 8–12 fold in height of a single CD (B-CD or G-CD), which might result from stacked-up of layers of B-G CDs except for the vast conjugation. In contrast, the AFM image (Fig. 7b) of B-G CDs (5:300) displays an even complex nanostructure. It is observed that the B-G CDs (5:300) became multi-ring structure with the height of around 6 nm, which is close to that of B-G CDs (5:30). This height might well denote B-G CD saturation associated with its conjugation in z-axis. In addition, SEM was performed on both B-G CDs (5:100 and 5:300) in the solid state, which appear as nanofibers. The average width of B-G CD (5:100) nanofibers is much narrower compared to that of B-G CD (5:300) nanofibers (Fig. 8a and b). Also, it was observed that the nanofibers had a tendency to self-assemble into nanosheets. Thus, based on different morphologies of B-G CDs obtained with different mass ratios, we hypothesize that the nanosheets originated from the conjugation of distinct CDs (B-CDs and G-CDs) to firstly generate figure-eight nanostructures, and then form nanofibers, which then self-assemble into nanosheets with single or multiple walls. A graphical illustration of the formation process into nanosheets is shown in Fig. S15.

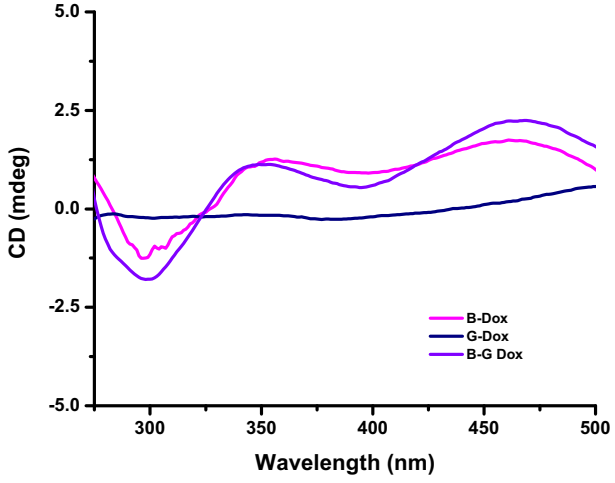

Fig. 5. Circular dichroism spectra of B-Dox (0.105 mg/mL), G-Dox (0.565 mg/mL), and B-G-Dox (0.165 mg/mL).

3.7. Bioimaging with a zebrafish model

Our research group has previously reported that B-CDs are promising biomaterials for bone specific imaging and drug delivery [19]. However, as a good drug nanocarrier, B-CDs cannot cross the BBB [23], which greatly limits their biomedical applications for

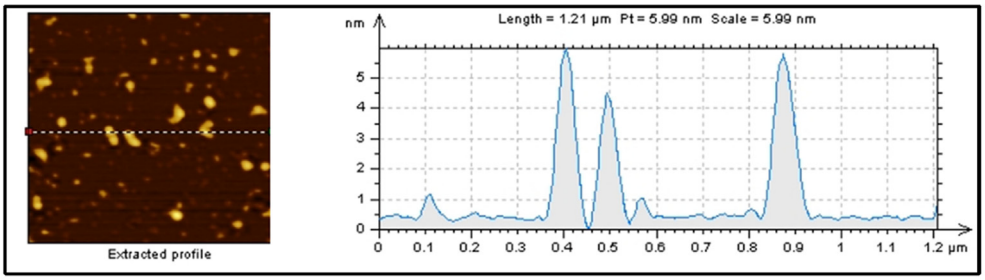

(a)

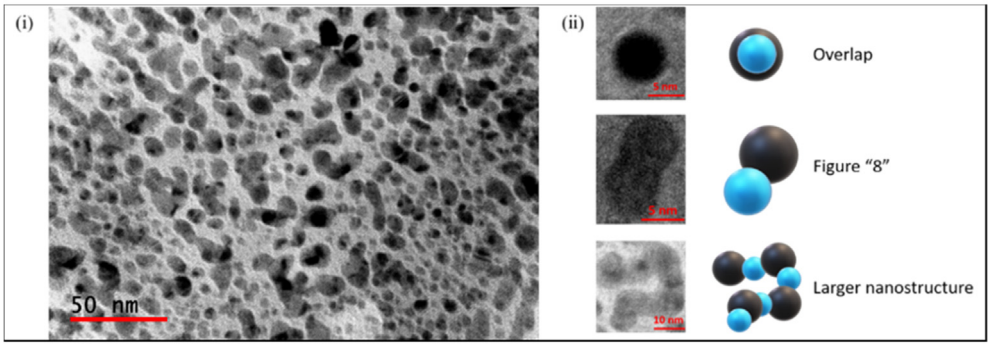

(b)

Fig. 6. (a) AFM and (b) TEM images of B-G CDs (5:30) (0.1 mg/ml). Scale bar in the TEM image represents 50 nm.

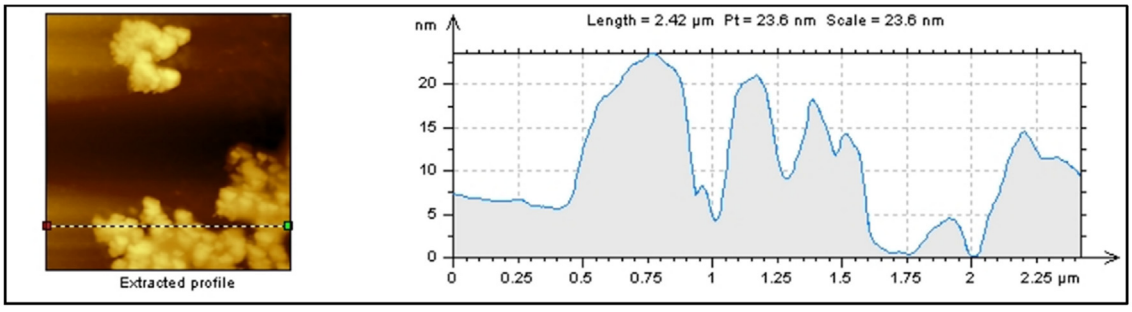

(a)

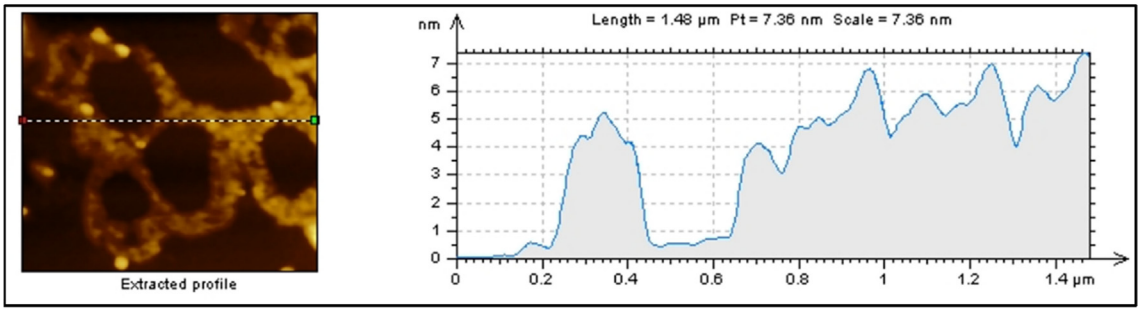

(b)

Fig. 7. AFM images of B-G CDs (a) (5:100), and (b) (5:300) (0.1 mg/ml).

central nervous system (CNS)-related diseases. In contrast, although G-CDs cannot target bones [19], they have exhibited the capability to cross the BBB, which is demonstrated in Fig. 10. Therefore, through conjugation, the unique biological properties of both B-CDs (bone targeting) and G-CDs (crossing the BBB) are expected to be passed on to the novel B-G CDs. In other words, both B-CDs and G-CDs can be considered as each other's "drug" and "drug nanocarrier" in B-G CDs, which will allow B-G CDs to

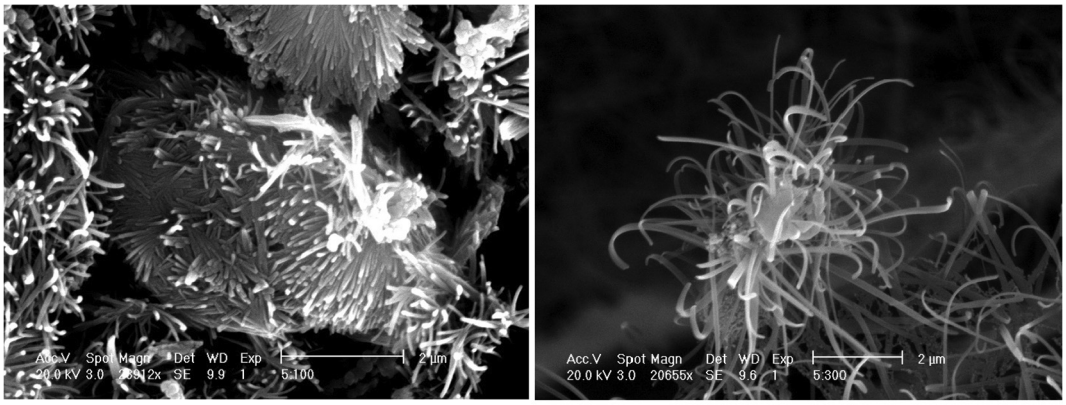

Fig. 8. SEM images of B-G CDs exhibiting different morphological patterns (a) (5:100), and (b) (5:300).

become a versatile drug nanocarrier for both targeting the bones while crossing the BBB. In addition, zebrafish was used as an *in vivo* model in this study for the following reasons: (1) compared to mice, it is more cost-effective to keep zebrafish since zebrafish don't need large space [23]; (2) adult zebrafish can breed every 10 days and produce 50–300 eggs, which can be used to repeat tests on bone targeting and crossing the BBB using B-G CDs, and yield robust results [51]. In contrast, during their entire lifetime, mice generally can only produce 5 litters. And for each litter, they can only bare up to 10 pups; (3) zebrafish larvae are nearly transparent, which is beneficial for the real-time bioimaging of tissue development and any fluorescently labeled activity in zebrafish body [52]. In contrast, mice pups are not transparent and have been well developed before birth; (4) zebrafish have similar and predictable skeleton and development of mineralizing tissues, which is close to those of humans [19]; (5) zebrafish have been widely applied as a *in vivo* model to investigate the BBB of humans and the treatment of diverse CNS-related diseases due to their genetic homology to humans [50]. Therefore, zebrafish served as the optimal *in vivo* model for this study.

B-CDs and B-G CDs (5:3, 5:30, 5:100 and 5:300) were separately injected into the yolk sac of anesthetized 7-day post-fertilization (7 dpf) zebrafish larvae (*Danio Rerio*) obtained from Zebrafish Core Facility at University of Miami. After 30 min, bioimaging under confocal microscope was performed. In Fig. 9a, bones including vertebrae, posterior branchiostegal ray, ceratobranchial 5, cleithrum and basioccipital articulatory process were observed in the larva injected with B-CDs under the excitation of 405 nm as was reported in our previous work [19]. In Fig. 9b, vertebrae were "lighted up" by excitation of 405 nm after various B-G CDs were injected even though the fluorescence gets less intense with B-G CDs (5:100) and (5:300), likely due to the decreasing relative content of B-CDs in the structure of B-G CDs along with the increasing amount of G-CDs that participate in the formation of B-G CDs (5:100 and 5:300). However, noteworthy is the fact that the test demonstrated that B-G CDs obtained the capability to target bones from B-CDs.

As a promising bone targeting nanocarrier, it is essential for B-G CDs to have a high surface NH_2 content to be able to load various bone disease-related drugs such as alendronate, risedronate, ibandronate and zoledronic acid. B-CDs do not contain —NH_2, which limits B-CDs' applications in the treatment of bone-related diseases. However, through conjugation with G-CDs, B-CDs gain —NH_2 on the surface. The quantification of —NH_2 on the surface

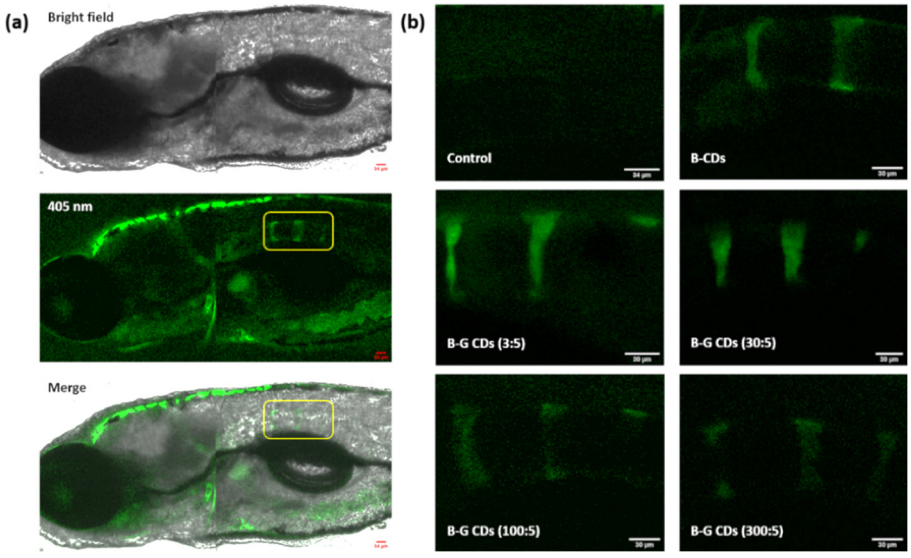

Fig. 9. Confocal images of zebrafish larvae (7 dpf) injected with B-CDs and various B-G CDs (5:3, 5:30, 5:100 and 5:300) at 100 mg/mL. (a) The zoomed out confocal images of the zebrafish larva after injection of B-CDs that show the vertebrae (circled in yellow); (b) bioimaging of vertebrae in the larvae injected with B-CDs and each type of B-G CDs. Each result was confirmed with 6 zebrafish larvae.

Table 1
Surface —NH_2 contents of B-G CDs obtained with different mass ratios.

B-CDs: G-CDs	5:3	5:30	5:100	5:300
—NH_2 content (mmol/mg)	1.68×10^{-2}	1.42×10^{-2}	1.46×10^{-2}	0.62×10^{-2}

of various B-G CDs was achieved via a fluorescamine-based fluorescence analysis, detailed more fully in our previous work [25]. Table 1 summarizes the —NH_2 content on the surfaces of various B-G CDs (5:3, 5:30, 5:100 and 5:300).

Furthermore, G-CDs and various B-G CDs were independently intravascularly injected into the heart of anesthetized zebrafish larvae (5 dpf). Each test was repeated with at least 6 zebrafish. After 10 min, the untreated and treated zebrafish were fixed on a glass plate using a low melting agar under a confocal microscope for bioimaging. To determine whether these NPs can cross the BBB, instead of directly scanning the brain, we chose to observe the central canal of spinal cord since the ventricle of the brain is connected to the central canal of spinal cord through the cerebral spinal fluid [23]. In order to reduce the interference of autofluorescence and considering the excitation-dependent PL of B-G CDs (Fig. 1a, S14b, S16), 405 nm was chosen as the excitation wavelength while the PL emission was collected ranging from 500 to 540 nm. Fig. 10 depicts that G-CDs and various B-G CDs were able to penetrate the BBB to reach the central canal of spinal cord. However, in comparison, it is clearly observed that G-CDs did not only exist inside the central canal, but also leak out, which suggests that the BBB penetration of G-CDs is due to a passive diffusion mechanism. Meanwhile, even though B-G CDs showed the capability to overcome the BBB, the mechanism cannot be attributed to passive diffusion because of their large particle size, high hydrophilicity and surface charge as revealed by their zeta potential value (Table 2). In terms of active routes, adsorption-mediated endocytosis and carrier-mediated transport is insufficient to explain the mechanism of B-G CD passage through the BBB considering their high negative surface charges and those of its precursors. Nonetheless, it was reported that polymers such as polysorbate 80 could adsorb plasma apolipoprotein E (Apo-E), which will cause the NPs coated with polysorbate 80 to be recognized as low-density lipoprotein (LDL) and help the uptake of NPs by the brain endothelial cells with the help of LDL receptors on these cells [53]. Considering the high surface charge and large surface area to volume ratio, B-G CDs are likely to adsorb Apo-E from plasma to be recognized as LDL. Thus, the more likely hypothesized mechanism for B-G CDs crossing the BBB is receptor-mediated endocytosis.

Therefore, the conjugation between B-CDs and G-CDs allows both properties (bone targeting and crossing the BBB) to be simultaneously revealed in the novel B-G CDs regardless of the mass ratio used for their conjugation, which allows the B-G CDs to become a versatile drug nanocarrier.

4. Conclusion

Although CDs are a promising new material, their supramolecular assembly has been lightly explored, and to the best of our knowledge have never been directly conjugated as a means of application optimization [29]. In this study, G-CDs and B-CDs were utilized as distinct CD models at a mass ratio of 5:3 for direct conjugation via an EDC/NHS mediated amidation reaction. After a two-step purification process, the formed B-G CDs (5:3) were characterized with various spectroscopic and microscopic measurements. AFM and TEM images revealed that the B-G CDs (5:3) are figure-eight shaped novel nanostructures. In addition, the conjugate inherits distinct merits from each individual CD. For instance, the

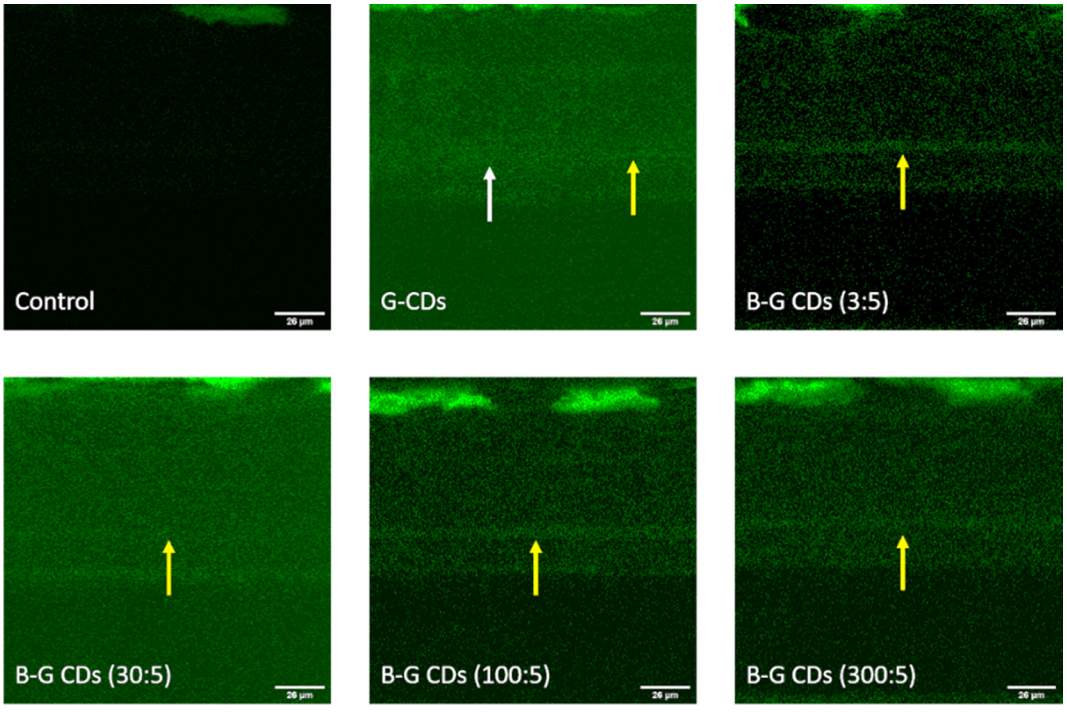

Fig. 10. Confocal images of the central canal of spinal cord of zebrafish larvae (5 dpf) injected intravascularly with G-CDs and various B-G CDs (5:3, 5:30, 5:100 and 5:300) independently at 100 mg/mL. Yellow arrows represent the central canal while the white arrow indicates the leakage of G-CDs. Each result was confirmed with 6 zebrafish larvae. (For interpretation of the references to colour in this figure legend, the reader is referred to the web version of this article.)

Table 2
Zeta potential measurement of B-G CDs obtained with different mass ratios.

B-CDs: G-CDs	5:3	5:30	5:100	5:300
Zeta potential (mV)	−31.6	−32.6	−29.3	−25.6

maximum excitation occurs blue shift while the corresponding emission occurs red shift in comparison to the PL of either B-CDs or G-CDs alone. FTIR and XPS measurements reveal the B-G CDs have diverse functionalities, which significantly broadens the application of B-G CDs as a drug nanocarrier. The increased functionality was also confirmed by a 54.5% increased drug loading capacity by circular dichroism spectroscopy with Dox as a drug model. Furthermore, the thermostability and aqueous stability have been improved as indicated by the increased decomposition temperature and zeta potential, respectively. Moreover, G-CDs were replaced by Y-CDs for conjugating with B-CDs without success, which indicates the importance of sufficient surface —NH_2 content for CDs' successful conjugation. Given the presence of —COOH on G-CDs, various physicochemical characterizations were performed to exclude the possibility of self-conjugation between G-CDs during the conjugation of B-CDs and G-CDs. Eventually, to test the ability of CDs to be used as building blocks in assembling novel nanostructures, the mass ratio for CDs conjugation was varied and novel nanostructures such as nanofibers and nanosheets were obtained, which were confirmed by AFM, TEM and SEM images. Moreover, these novel nanostructures of B-G CDs (5:3, 5:30, 5:100 and 5:300) have shown combined properties of bone targeting and the ability to cross the BBB by B-CDs and G-CDs, respectively with zebrafish as an *in vivo* model. This dual-targeting property has not been reported in the literature for CDs to the best of our knowledge. We proposed the idea of improving CDs' properties through covalent conjugation of distinct CDs. This has been proven through the increased drug loading efficiency of B-G CDs as compared to the individual CDs, and ability to target both the bones and CNS in zebrafish. Therefore, CDs prove to be promising Lego-like building blocks for the assembly of novel, versatile drug nanocarriers. In the future, we expect that many useful properties relating to surface functionality, optics, and drug delivery will be combined in the manner described in this article to maximize applications of these CDs.

CRediT authorship contribution statement

Yiqun Zhou: Conceptualization, Methodology, Validation, Formal analysis, Investigation, Data curation, Writing - original draft, Writing - review & editing, Visualization, Project administration. **Keenan J. Mintz:** Methodology, Validation, Investigation, Data curation, Writing - review & editing, Visualization. **Ling Cheng:** Methodology, Validation, Formal analysis, Investigation, Writing - review & editing. **Jiuyan Chen:** Validation, Formal analysis, Investigation, Writing - review & editing. **Braulio C.L.B. Ferreira:** Validation, Formal analysis, Investigation, Writing - review & editing, Visualization. **Sajini D. Hettiarachchi:** Conceptualization, Methodology, Formal analysis, Investigation, Writing - review & editing. **Piumi Y. Liyanage:** Conceptualization, Validation, Formal analysis, Investigation, Writing - review & editing, Visualization. **Elif S. Seven:** Investigation, Writing - review & editing, Visualization. **Nikolay Miloserdov:** Validation, Formal analysis, Investigation. **Raja R. Pandey:** Validation, Formal analysis, Investigation, Visualization. **Bruno Quiroga:** Methodology, Investigation. **Patricia L. Blackwelder:** Validation, Formal analysis, Investigation, Resources, Data curation, Writing - review & editing, Visualization. **Charles C. Chusuei:** Conceptualization, Validation, Formal analysis, Investigation, Resources, Data curation, Writing - review & editing, Visualization. **Shanghao Li:** Conceptualization, Resources, Writing - review & editing. **Zhili Peng:** Writing - review & editing, Supervision, Funding acquisition. **Roger M. Leblanc:** Conceptualization, Methodology, Resources, Data curation, Writing - review & editing, Supervision, Project administration, Funding acquisition.

Declaration of Competing Interest

The authors declare no competing financial interests or personal relationships that could have appeared to influence the work reported in this paper.

Acknowledgment

Professor Roger M. Leblanc thanks the National Science Foundation for support under the grant 011298. The authors gratefully acknowledge support from King Abdulaziz University, Kingdom of Saudi Arabia, and the University of Miami, USA. Professor Zhili Peng acknowledges financial support from the National Natural Science Foundation of China under grant 21807010, the Applied Basic Research Program of Yunnan Province (No. 2019FB066) and the "Double-First Class" University Construction Project (C176220200040) of Yunnan University.

Appendix A. Supplementary materia

Supplementary data to this article can be found online at https://doi.org/10.1016/j.jcis.2020.05.005.

References

[1] Y. Zhou, S.K. Sharma, Z. Peng, R.M. Leblanc, Polymers in carbon dots: A review, Polymers 9 (2017) 67–86.
[2] S. Mandani, D. Dey, B. Sharma, T.K. Sarma, Natural occurrence of fluorescent carbon dots in honey, Carbon 119 (2017) 569–572.
[3] R. Ludmerczki, S. Mura, C.M. Carbonaro, I.M. Mandity, M. Carraro, N. Senes, S. Garroni, G. Granozzi, L. Calvillo, S. Marras, L. Malfatti, P. Innocenzi, Carbon dots from citric acid and its intermediates formed by thermal decomposition, Chem.: Eur. J. 25 (2019) 11963–11974.
[4] M. Javed, A.N.S. Saqib, R. Ata ur, B. Ali, M. Faizan, D.A. Anang, Z. Iqbal, S.M. Abbas, Carbon quantum dots from glucose oxidation as a highly competent anode material for lithium and sodium-ion batteries, Electrochim. Acta 297 (2019) 250–257.
[5] M.L. Liu, B.B. Chen, C.M. Li, C.Z. Huang, Carbon dots: Synthesis, formation mechanism, fluorescence origin and sensing applications, Green Chem. 21 (2019) 449–471.
[6] Y. Wang, A. Hu, Carbon quantum dots: Synthesis, properties and applications, J. Mater. Chem. C 2 (2014) 6921–6939.
[7] Z. Peng, X. Han, S. Li, A.O. Al-Youbi, A.S. Bashammakh, M.S. El-Shahawi, R.M. Leblanc, Carbon dots: Biomacromolecule interaction, bioimaging and nanomedicine, Coord. Chem. Rev. 343 (2017) 256–277.
[8] K. Jiang, S. Sun, L. Zhang, Y. Lu, A. Wu, C. Cai, H. Lin, Red, green, and blue luminescence by carbon dots: Full-color emission tuning and multicolor cellular imaging, Angew. Chem. Int. Ed. 54 (2015) 5360–5363.
[9] L. Song, Y. Cui, C. Zhang, Z. Hu, X. Liu, Microwave-assisted facile synthesis of yellow fluorescent carbon dots from o-phenylenediamine for cell imaging and sensitive detection of Fe^{3+} and H_2O_2, RSC Adv. 6 (2016) 17704–17712.
[10] T. Kong, L. Hao, Y. Wei, X. Cai, B. Zhu, Doxorubicin conjugated carbon dots as a drug delivery system for human breast cancer therapy, Cell Prolif. 51 (2018) e12488–e12496.
[11] K.O. Boakye-Yiadom, S. Kesse, Y. Opoku-Damoah, M.S. Filli, M. Aquib, M.M.B. Joelle, M.A. Farooq, R. Mavlyanova, F. Raza, R. Bavi, B. Wang, Carbon dots: Applications in bioimaging and theranostics, Int. J. Pharm. 564 (2019) 308–317.
[12] X. Sun, Y. Lei, Fluorescent carbon dots and their sensing applications, Trends Anal. Chem. 89 (2017) 163–180.
[13] K. Nakano, T. Honda, K. Yamasaki, Y. Tanaka, K. Taniguchi, R. Ishimatsu, T. Imato, Carbon quantum dots as fluorescent component in peroxyoxalate chemiluminescence for hydrogen peroxide determination, Bull. Chem. Soc. Jpn. 91 (2018) 1128–1130.
[14] X. Miao, D. Qu, D. Yang, B. Nie, Y. Zhao, H. Fan, Z. Sun, Synthesis of carbon dots with multiple color emission by controlled graphitization and surface functionalization, Adv. Mater. 30 (2018) 1704740–1704747.
[15] M. Han, S. Zhu, S. Lu, Y. Song, T. Feng, S. Tao, J. Liu, B. Yang, Recent progress on the photocatalysis of carbon dots: Classification, mechanism and applications, Nano Today 19 (2018) 201–218.

[16] C.-F. Wang, R. Cheng, W.-Q. Ji, K. Ma, L. Ling, S. Chen, Recognition of latent fingerprints and ink-free printing derived from interfacial segregation of carbon dots, ACS Appl. Mater. Interfaces 10 (2018) 39205–39213.
[17] E.S. Seven, S.K. Sharma, D. Meziane, Y. Zhou, K.J. Mintz, R.R. Pandey, C.C. Chusuei, R.M. Leblanc, Close-packed langmuir monolayers of saccharide-based carbon dots at the air–subphase interface, Langmuir 35 (2019) 6708–6718.
[18] D.-W. Zheng, B. Li, C.-X. Li, J.-X. Fan, Q. Lei, C. Li, Z. Xu, X.-Z. Zhang, Carbon-dot-decorated carbon nitride nanoparticles for enhanced photodynamic therapy against hypoxic tumor via water splitting, ACS Nano 10 (2016) 8715–8722.
[19] Z. Peng, E.H. Miyanji, Y. Zhou, J. Pardo, S.D. Hettiarachchi, S. Li, P.L. Blackwelder, I. Skromne, R.M. Leblanc, Carbon dots: Promising biomaterials for bone-specific imaging and drug delivery, Nanoscale 9 (2017) 17533–17543.
[20] Y. Zhou, K.J. Mintz, C.Y. Oztan, S.D. Hettiarachchi, Z. Peng, E.S. Seven, P.Y. Liyanage, S. De La Torre, E. Celik, R.M. Leblanc, Embedding carbon dots in superabsorbent polymers for additive manufacturing, Polymers 10 (2018) 921–932.
[21] Y. Zhou, A. Desserre, S.K. Sharma, S. Li, M.H. Marksberry, C.C. Chusuei, P.L. Blackwelder, R.M. Leblanc, Gel-like carbon dots: Characterization and their potential applications, ChemPhysChem 18 (2017) 890–897.
[22] S. Li, L. Wang, C.C. Chusuei, V.M. Suarez, P.L. Blackwelder, M. Micic, J. Orbulescu, R.M. Leblanc, Nontoxic carbon dots potently inhibit human insulin fibrillation, Chem. Mater. 27 (2015) 1764–1771.
[23] S. Li, Z. Peng, J. Dallman, J. Baker, A.M. Othman, P.L. Blackwelder, R.M. Leblanc, Crossing the blood–brain–barrier with transferrin conjugated carbon dots: A zebrafish model study, Colloids Surf. B 145 (2016) 251–256.
[24] S. Li, I. Skromne, Z. Peng, J. Dallman, A.O. Al-Youbi, A.S. Bashammakh, M.S. El-Shahawi, R.M. Leblanc, "Dark" carbon dots specifically "light-up" calcified zebrafish bones, J. Mater. Chem. B 4 (2016) 7398–7405.
[25] Y. Zhou, P.Y. Liyanage, D.L. Geleroff, Z. Peng, K.J. Mintz, S.D. Hettiarachchi, R.R. Pandey, C.C. Chusuei, P.L. Blackwelder, R.M. Leblanc, Photoluminescent carbon dots: A mixture of heterogeneous fractions, 19 (2018) 2589–2597.
[26] P.J. Santos, Z. Cao, J. Zhang, A. Alexander-Katz, R.J. Macfarlane, Dictating nanoparticle assembly via systems-level control of molecular multivalency, J. Am. Chem. Soc. 141 (2019) 14624–14632.
[27] M. Niederberger, Multiscale nanoparticle assembly: From particulate precise manufacturing to colloidal processing, 27 (2017) 1703647–1703664.
[28] T. Wang, D. LaMontagne, J. Lynch, J. Zhuang, Y.C. Cao, Colloidal superparticles from nanoparticle assembly, Chem. Soc. Rev. 42 (2013) 2804–2823.
[29] Y. Liu, Z.-Y. Zhang, S.-D. Nie, C.-Y. Liu, Luminescence modulation of carbon dots assemblies, J. Mater. Chem. C 7 (2019) 6337–6343.
[30] S. Li, D. Amat, Z. Peng, S. Vanni, S. Raskin, G. De Angulo, A.M. Othman, R.M. Graham, R.M. Leblanc, Transferrin conjugated nontoxic carbon dots for doxorubicin delivery to target pediatric brain tumor cells, Nanoscale 8 (2016) 16662–16669.
[31] Y. Ji, Y. Zhou, E. Waidely, A. Desserre, M.H. Marksberry, C.C. Chusuei, A.A. Dar, O.A. Chat, S. Li, R.M. Leblanc, Rheology of a carbon dot gel, Inorganica Chim. Acta 468 (2017) 119–124.
[32] K.J. Mintz, G. Mercado, Y. Zhou, Y. Ji, S.D. Hettiarachchi, P.Y. Liyanage, R.R. Pandey, C.C. Chusuei, J. Dallman, R.M. Leblanc, Tryptophan carbon dots and their ability to cross the blood-brain barrier, Colloids Surf. B 176 (2019) 488–493.
[33] C.D. Wagner, L.E. Davis, M.V. Zeller, J.A. Taylor, R.H. Raymond, L.H. Gale, Empirical atomic sensitivity factors for quantitative analysis by electron spectroscopy for chemical analysis, Surf. Interface Anal. 3 (1981) 211–225.
[34] D.A. Shirley, High-resolution x-ray photoemission spectrum of the valence bands of gold, Phys. Rev. B 5 (1972) 4709–4714.
[35] Y. Zhou, K.J. Mintz, S.K. Sharma, R.M. Leblanc, Carbon dots: Diverse preparation, application, and perspective in surface chemistry, Langmuir 35 (2019) 9115–9132.
[36] S.Y. Madani, F. Shabani, M.V. Dwek, A.M. Seifalian, Conjugation of quantum dots on carbon nanotubes for medical diagnosis and treatment, Int. J. Nanomedicine 8 (2013) 941–950.
[37] K.F. Chou, A.M. Dennis, Förster resonance energy transfer between quantum dot donors and quantum dot acceptors, Sensors (Basel) 15 (2015) 13288–13325.
[38] K. Yang, F. Li, W. Che, X. Hu, C. Liu, F. Tian, Increment of the FRET efficiency between carbon dots and photosensitizers for enhanced photodynamic therapy, RSC Adv. 6 (2016) 101447–101451.
[39] B. Yu, X. Wang, X. Qian, W. Xing, H. Yang, L. Ma, Y. Lin, S. Jiang, L. Song, Y. Hu, S. Lo, Functionalized graphene oxide/phosphoramide oligomer hybrids flame retardant prepared via in situ polymerization for improving the fire safety of polypropylene, RSC Adv. 4 (2014) 31782–31794.
[40] P.Y. Liyanage, R.M. Graham, R.R. Pandey, C.C. Chusuei, K.J. Mintz, Y. Zhou, J.K. Harper, W. Wu, A.H. Wikramanayake, S. Vanni, R.M. Leblanc, Carbon nitride dots: A selective bioimaging nanomaterial, Bioconjugate Chem. 30 (2019) 111–123.
[41] Y. Liu, Y. Liu, S.-J. Park, Y. Zhang, T. Kim, S. Chae, M. Park, H.-Y. Kim, One-step synthesis of robust nitrogen-doped carbon dots: acid-evoked fluorescence enhancement and their application in Fe^{3+} detection, J. Mater. Chem. A 3 (2015) 17747–17754.
[42] Y. Zhou, E.M. Zahran, B.A. Quiroga, J. Perez, K.J. Mintz, Z. Peng, P.Y. Liyanage, R. R. Pandey, C.C. Chusuei, R.M. Leblanc, Size-dependent photocatalytic activity of carbon dots with surface-state determined photoluminescence, Appl. Catal. B 248 (2019) 157–166.
[43] G. Huang, X. Chen, C. Wang, H. Zheng, Z. Huang, D. Chen, H. Xie, Photoluminescent carbon dots derived from sugarcane molasses: synthesis, properties, and applications, RSC Adv. 7 (2017) 47840–47847.
[44] A. Mewada, S. Pandey, M. Thakur, D. Jadhav, M. Sharon, Swarming carbon dots for folic acid mediated delivery of doxorubicin and biological imaging, J. Mater. Chem. B 2 (2014) 698–705.
[45] D. Wang, Z. Wang, Q. Zhan, Y. Pu, J.-X. Wang, N.R. Foster, L. Dai, Facile and scalable preparation of fluorescent carbon dots for multifunctional applications, Engineering 3 (2017) 402–408.
[46] A. Mewada, S. Pandey, S. Shinde, N. Mishra, G. Oza, M. Thakur, M. Sharon, M. Sharon, Green synthesis of biocompatible carbon dots using aqueous extract of Trapa bispinosa peel, Mater. Sci. Eng. C 33 (2013) 2914–2917.
[47] X. Gong, Q. Zhang, Y. Gao, S. Shuang, M.M.F. Choi, C. Dong, Phosphorus and nitrogen dual-doped hollow carbon dot as a nanocarrier for doxorubicin delivery and biological imaging, ACS Appl. Mater. Interfaces 8 (2016) 11288–11297.
[48] A. Vassilakopoulou, V. Georgakilas, N. Vainos, I. Koutselas, Successful entrapment of carbon dots within flexible free-standing transparent mesoporous organic-inorganic silica hybrid films for photonic applications, J. Phys. Chem. Solids 103 (2017) 190–196.
[49] A.B. Bourlinos, R. Zbořil, J. Petr, A. Bakandritsos, M. Krysmann, E.P. Giannelis, Luminescent surface quaternized carbon dots, Chem. Mater. 24 (2012) 6–8.
[50] Y. Zhou, P.Y. Liyanage, D. Devadoss, L.R. Rios Guevara, L. Cheng, R.M. Graham, H.S. Chand, A.O. Al-Youbi, A.S. Bashammakh, M.S. El-Shahawi, R.M. Leblanc, Nontoxic amphiphilic carbon dots as promising drug nanocarriers across the blood–brain barrier and inhibitors of β-amyloid, Nanoscale 11 (2019) 22387–22397.
[51] A. Avdesh, M. Chen, M.T. Martin-Iverson, A. Mondal, D. Ong, S. Rainey-Smith, K. Taddei, M. Lardelli, D.M. Groth, G. Verdile, R.N. Martins, Regular care and maintenance of a zebrafish (Danio rerio) laboratory: an introduction, J. Vis. Exp. 69 (2012) e4196–e4203.
[52] J.R. Meyers, Zebrafish: Development of a vertebrate model organism, Curr. Protoc. 16 (2018) e19–e44.
[53] Y. Zhou, Z. Peng, E.S. Seven, R.M. Leblanc, Crossing the blood-brain barrier with nanoparticles, J. Control. Release 270 (2018) 290–303.